energies

MDPI

Article

Design for a Heat Pump with Sink Temperatures of 200 °C Using a Radial Compressor

Julian Unterluggauer [1,*], Verena Sulzgruber [1], Clemens Kroiss [2], Johannes Riedl [1], Reinhard Jentsch [1] and Reinhard Willinger [2,*]

[1] Center for Energy, Austrian Institute of Technology, 1210 Vienna, Austria; verena.sulzgruber@ait.ac.at (V.S.); johannes.riedl@ait.ac.at (J.R.); reinhard.jensch@ait.ac.at (R.J.)
[2] Institute of Energy Systems and Thermodynamics, TU Wien, 1060 Vienna, Austria; clemens.kroiss@gmx.at
* Correspondence: julian.unterluggauer@ait.ac.at (J.U.); reinhard.willinger@tuwien.ac.at (R.W.)

Abstract: To reduce CO_2 emissions in the industrial sector, high-temperature heat pumps are a key technology. This work presents an approach to design such an industrial heat pump system capable of supplying 200 °C sink temperature and a capacity of approximately 1 MW. Today's market-available heat pumps using displacement compressors are not suitable for reaching that high sink temperatures as they need lubricating oil, which is not temperature resistant enough. As a consequence, in this study a transcritical heat pump cycle using a two-stage oil-free radial compressor is investigated. Based on preliminary studies, R1233zd(E) is chosen as a refrigerant. The procedure couples 1D thermodynamic cycle simulations with a radial compressor mean-line design model. A preliminary geometry for a compressor with and without inlet guide vanes is presented, and compressor maps including the compressors behaviour in off-design are calculated. The compressor design is then imported into a 1D simulation to analysis the performance of the heat pump in the whole operating range. In the analysis, the application of a fixed inlet is evaluated, and an improvement of approximately 21% and 16% of the isentropic efficiency is achieved. The thermodynamic simulations showed a maximum COP of approximately 2.8 and a possible operating range of 0.5 to 1.3 MW thermal power. Furthermore, a techno-economical analysis by means of a deep-fryer use case showed reasonable payback times of between 2 and 10 years, depending on the electricity to gas price ratio.

Keywords: high-temperature heat pump; radial compressor; simulation

Citation: Unterluggauer, J.; Sulzgruber, V.; Kroiss, C.; Riedl, J.; Jentsch, R.; Willinger, R. Design for a Heat Pump with Sink Temperatures of 200 °C Using a Radial Compressor. *Energies* **2023**, *16*, 4916. https://doi.org/10.3390/en16134916

Academic Editor: Annunziata D'Orazio

Received: 23 May 2023
Revised: 16 June 2023
Accepted: 21 June 2023
Published: 24 June 2023

1. Introduction

Nowadays, the industrial sector is undergoing significant changes to reduce CO_2 emissions and mitigate its impact on climatic change. The European Union is aiming at CO_2 neutrality by 2050 and reducing total greenhouse gas emissions by 55% by 2030, as stated in the 2030 Climate & Energy Framework [1]. Heat required for homes, industry and other applications is the largest energy end-use, accounting for around half of total energy consumption [2]. Therefore, the decarbonization of this sector is of key interest for society. In all those sectors, heat pumps are going to play a major role to boost low-to-medium temperature levels up to higher ones by means of electricity. Industrial waste heat across the whole temperature band is estimated to be approximately 300 TWh/year [3] in the EU. However, for heat pumps it is crucial to limit the waste heat to a maximum of approximately 100–120 °C as, at this source temperature, other technologies, such as organic Rankine cycle (ORC) [4] might be advantageous. Thus, the actual heat production potential in EU industries has to be reduced to 28.37 TWh/year [5]. Kosmadakis [6] evaluated the potential of industrial high-temperature heat pumps for sink temperatures of above 100 °C. The heat demand in the EU in the 100–500 °C temperature range for different industries is presented in Figure 1. Kosmadakis [6] came to the final conclusion that the 100–200 °C temperature range is of particular interest, as it represents 15% of the total heat consumption.

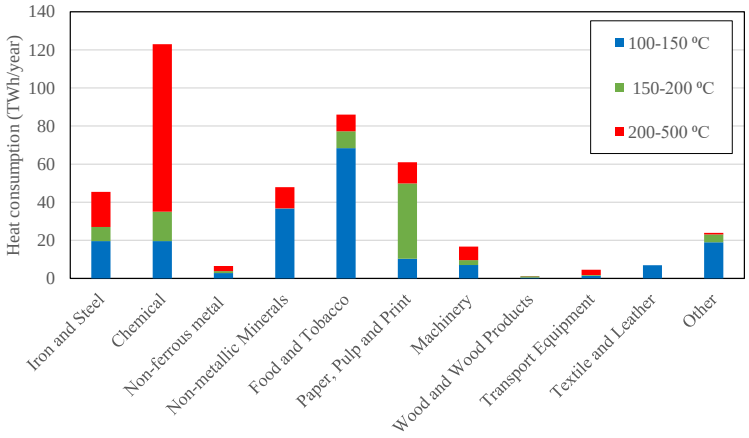

Figure 1. Heat demand in the EU between 100 °C and 500 °C [6].

Today's market-available high-temperature heat pumps are capable of producing constant sink temperatures of approximately 120 °C, with maximum temperatures of approximately 130 °C [7]. Higher sink temperatures are possible but still subject to research. The performance of the heat pump cycle together with the refrigerant, which is, in this case, for most substances operating above the critical point, is still a question of debate. However, some research activities targeting temperature levels above 150 °C [8,9] showed that it is quite challenging to find a compressor and lubricating oil that can withstand those high temperatures [10]. Therefore, an oil-free compressor solution would be able to target even higher temperatures. Compared to positive displacement compressors, radial turbo compressors bear this key advantage, along with high efficiency and a compact design. In large heat pumps for district heat systems, radial compressors are currently the number one option. However, smaller units significantly beneath 2 MW electrical power are required for typical industrial processes, with capacities between 0.5 and 2 MW thermal power. Decreasing the size leads to lower efficiencies and most crucially higher rotational speeds, which makes them currently not available on the market. The progress in the last few decades in the development and design of high-speed motors [11] has already supported the use of the radial compressor application in refrigeration. For example, Schiffmann and Favrat [12] developed a small scale turbo compressor for domestic heat pump applications with a rotational speed of 210 krpm and internal total-to-total isentropic compressor efficiencies of up to 79%. Moreover, Hanslik [13] conducted research on small radial compressors for refrigeration systems operating up to 90 krpm and achieving an overall efficiency of 70%. Meroni et al. [14] investigated compressor designs for high-temperature applications. In their use case, which assumed the heat pump to supply process steam at 150 °C, an open loop with water as a refrigerant was found to be the most promising solution. For the evaluation whether or not a suitable radial compressor design for specified heat pump operating conditions can be found, a design method that is fast and robust is needed. Harley et al. [15] pointed out that the 1D single-zone method is most suitable for the preliminary design process of radial compressors.

In this article, a design process for a heat pump with approximately 1 MW thermal power and sink temperatures of approximately 200 °C will be presented. In contrast to the work of Meroni et al. [14], the goal is not to produce steam but to heat up oil, air or theoretically pressurized water. This highlights the novelty of the study as investigations on closed-loop circuits for temperatures above or around 200 °C are rare. Moreover, the design model is focusing on transcritical heat pump cycles, because for most refrigerants the critical point lies beneath 200 °C. The refrigerant behaviour at high temperatures has already been investigated in the literature, but a design concept for a whole heat pump including a real use-case is still missing.

2. Methodology

Figure 2 shows the methodology of the heat pump design process. The operation conditions are first determined, refrigerants are selected and an optimisation with the goal to maximise the COP is performed. The isentropic efficiency is thereby assumed to be constant at approximately 0.75.

The most suitable options are than passed to the preliminary design process of the compressor, which is explained in the following chapter. With a suitable design of the compressor, heat pump simulations for a close to reality use case can be carried out, and the concept can be evaluated.

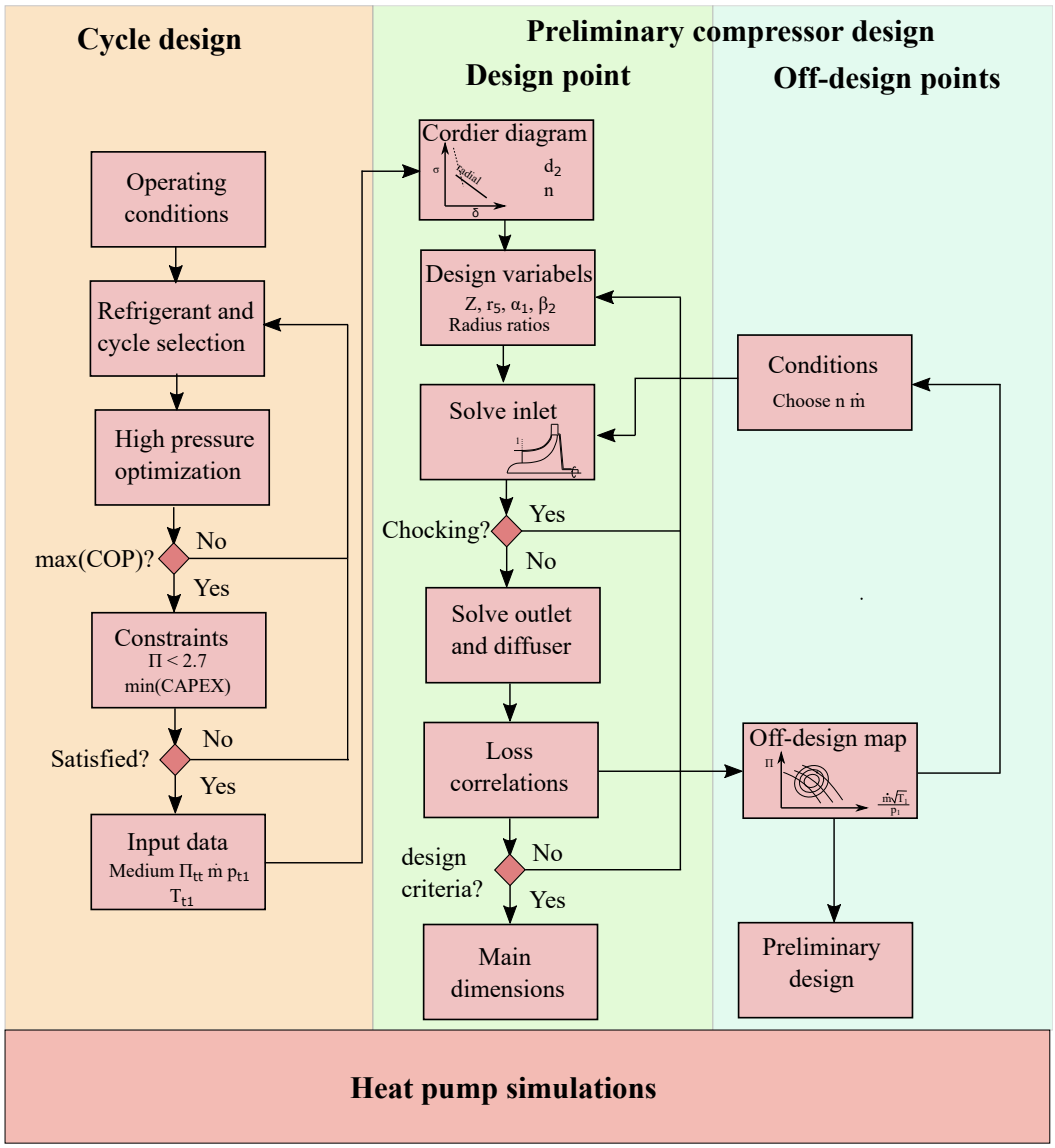

Figure 2. Preliminary design process for the high-temperature heat pump.

2.1. Heat Pump Model

A flow diagram of the investigated heat pump cycle is depicted in Figure 3. As more complex cycles including flow injection between the compressor stages proved to be disadvantageous regarding the overall COP of the heat pump [16], a simple cycle including only an internal heat exchanger (HEX) is used. The operating conditions at the design point are summarized in Table 1.

The heat pump cycle, including the required components such as compressors and vessels, is modelled using the acausal object-oriented, equation-based open-source mod-

elling language Modelica. Dymola 2022x is used as a simulation environment with basic components such ad HEX or expansion valve from the commercial library TIL 3.10.0, developed by TLK Thermo GmbH. The thermophysical properties of the working media are taken from the fluid database in TILMedia, supplemented with the help of the tool REFPROP 10 [17]. Refrigerant mixtures are modelled with splines to ensure numerical stability and to speed up the calculations. The maximum error is approximately 3% near the critical point, and in most points even a power of ten beneath. To keep the simulations as simple and comparable as possible, the following simplifications are made:

- Neglect pressure losses (e.g., pipes);
- Constant super heating of 0.1 °C at the outlet of the evaporator;
- Oversized HEX to minimize the influence of heat transfer and heat-transfer coefficients;
- Neglect thermal losses.

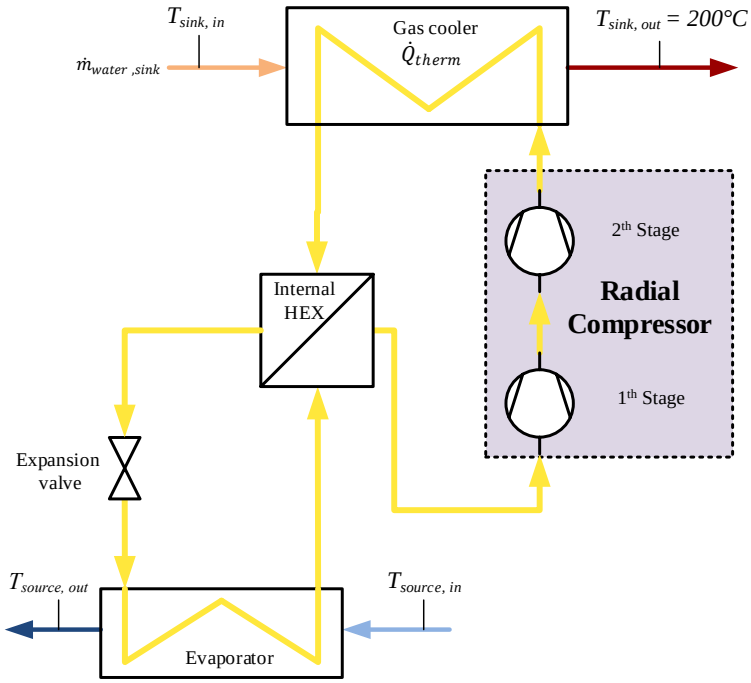

Figure 3. Flow diagram of the investigated heat pump cycle.

Table 1. Operating conditions at design point.

Designation	Abbreviation	Value
Thermal power	$\dot{Q}_{therm}$	1 MW_{th}
Sink temperature (outlet)	$T_{sink,out}$	200 °C
Sink temperature spread	ΔT_{sink}	40 °C
Source temperature (inlet)	$T_{source,in}$	95 °C
Source temperature spread	ΔT_{source}	5 °C
Evaporation temperature	T_{evap}	90 °C
Temperature difference in internal HEX	ΔT_{pinch}	15 °C

2.2. Refrigerant

To find suitable refrigerants for the desired temperature range, commonly used fluids are scanned regarding their temperature stability and general technical feasibility [16]. Moreover, ozone depletion potential (ODP), global warming potential (GWP), ASHREA safety class, volumetric heating capacity and required system pressure are also considered. In Table 2, the pre-selection of natural and synthetic refrigerant, as well as certain mixtures,

are shown. Water (R718) as a refrigerant generally has sufficient properties, especially from a safety and environmental point of view. However, for the desired temperature range and application, the advantages of the other refrigerants are valued higher, as already discussed in Helminger et al. [18]. Ammonia (R717) is known for its good performance as a refrigerant in terms of a high volumetric capacity, but the high pressure needed for temperatures above 100 °C makes it infeasible if costs for equipment such as valves and vessels are taken into account.

The presented mixtures are based on the fact that R601 (Pentane) showed the best COP performance, but with the downside of a high pressure ratio for the compressor in preliminary calculations [18]. The components and fractions are based on Fernández-Moreno et al. [19], who were investigating the possibility of various mixtures for a sink temperature of 140 °C. However, the results were checked in accordance with preliminary calculations and expected performance of the blends, and two of those mixtures were identified as promising for the desired temperature range.

Table 2. Refrigerant selection.

Refrigerant	γ	T_{Crit}	ODP	GWP	Safety Class	T_{De}
R1233zd(E)	1	166.4	0	1	A1	277
R1336mzz(Z)	1	171.3	0	2	A1	>250
R1336mzz(E)	1	137.7	0	18	A1	>250
R601 (Pentane)	1	196.5	0	5	A3	376
Cyclopentane	1	238.5	0	5	A3	275
R600 (n-Butane)	1	152.0	0	4	A3	302
R601/1234ze(Z)	0.74/0.26	180.8	0	5.6	A3	n.a.
R1233zd(E)/601/152	0.65/0.25/0.1	165.5	0	14.4	A2L	n.a.

2.3. Compressor Design Model

In this work, a steady-state, mean-line approach is used to design the radial compressor. The model is written in Python, and the flow as well as the thermodynamic conditions are calculated at mid-span in the compressors meridian view. All these values represent mass-weighted averaged conditions over the whole section. The model focuses on the runner, but a vaneless radial diffuser and the possibility of inlet guide vanes are also taken into account. In the case of the fluid properties, real-gas equations of state are used by including the thermodynamic libraries CoolProp [20] and REFPROP version 10 [21]. To determine the flow and thermodynamic conditions at various important stations along the mean-line, the energy balance, mass continuity and loss equations are solved iteratively. Furthermore, to find a suitable design for a given operating point, chocking has to be prevented. This means that, locally, speed of sound is reached and shock-waves lead to a decrease of the mass flow and an obvious drop in efficiency. Chocking will most likely occur in the runner passage or at the point of minimum flow area [22] and is directly influenced by the rotational speed.

A schematic overview including the most important geometrical design parameters can be seen in Figure 4.

To begin, a refrigerant as well as a desired total pressure ratio, Π_{tt}, for the compressor has to be chosen. This pressure ratio,

$$\Pi_{tt} = \frac{p_{t5}}{p_{t1}}, \tag{1}$$

is calculated by using the runner inlet and diffuser outlet section. Accordingly, total inlet pressure, p_{t1}, total temperature, T_{t1}, and the mass flow, $\dot{m}$, have to be specified. With these boundaries, an outlet diameter, d_2, and rotation speed, n, are determined using the Cordier diagram [23]. This classification guideline for the type of turbomachinery (axial, mixed or radial) is based on an intensive empirical analysis of proved geometry using extensive experimental data. However, Willinger [24] also showed that the shape of the Cordier lines

also depend on the energy conversion of the fan or compressor. In the next step, additional design variables have to be chosen. Thereby, the radius ratios and the relative outlet blade angle, β_{2b}, have to be determined according to Table 3. Moreover, an absolute inlet flow angle, α_1, which is bigger than 0° if inlet guide vanes are used, has to be defined. All angels are defined based on the rotating axis of the impeller. As the circumferential component is defined as positive, according to the rotation of the impeller, stator parts will always have positive angles, while the rotor angels will be negative.

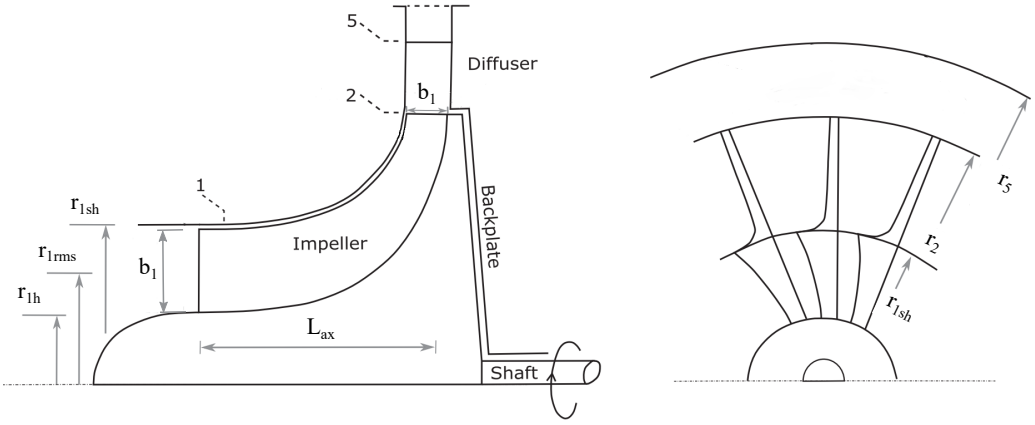

Figure 4. Main dimensions of the radial compressor.

Table 3. Design parameter ratios.

Name	Variable	Lower Boundary	Upper Boundary
Inlet shroud to tip radius ratio	$\frac{r_{1sh}}{r_2}$	0.4	0.7
Inlet hub to shroud radius ratio	$\frac{r_{1h}}{r_{1sh}}$	0.25	0.7
Flow angle guide vane	α_1	0°	30°
Outlet blade angle	β_{2b}	−45°	0°

The last remaining variable is the number of runner blades, Z. Since the early days of fluid machinery, this is one of the most discussed design parameters. On one hand, a higher number of blades causes low blade loading but results in higher friction losses. On the other hand, a lower number of blades leads to a higher blade loading, resulting in higher friction losses due to increased secondary flow and stronger deviation between flow and actual blade direction. Therefore, many rules of thumb exist to at least get a good grasp on how many blades would be sufficient. One of the most well known is the one presented by Pfleiderer [25]

$$Z = k_z \left(\frac{d_2 + d_1}{d_2 - d_1} \right) \sin \left(\frac{\beta_{1b} - \beta_{2b}}{2} \right) \tag{2}$$

with the material factor k_z = 6.5–8 for compressors. However, as the inlet blade angle is a result of the calculation, a correlation based on only the input parameters would be beneficial. Therefore, an empirical approach based on the data of Xu et al. [26] and also discussed by Meroni et al. [14] is considered. The number of runner blades, Z, is depending on Π_{tt} and determined as

$$Z = 12.03 + 2.544 \Pi_{tt} \tag{3}$$

and for the application of splitter blades

$$Z = -4.527 e^{\left(\frac{1.865}{\Pi_{tt}} \right)} + 32.22 \tag{4}$$

The number is than rounded to the nearest integer value to obtain a viable starting point.

Besides these additional variable parameters, there are some design parameters (Table 4) that are assumed to be fixed. For the tip clearance, the equation of Traupel [27] can be used

$$\epsilon_{tip} = 0.6\frac{d_2}{1000} + 0.25 \text{ mm} \tag{5}$$

Table 4. Additional design parameters.

Name	Variable	Value
Blade thickness hub	t_{bh}	1.9 mm
Blade thickness shroud	t_{bs}	0.7 mm
Shroud clearance	ϵ	0.15 mm
Back face clearance	ϵ_{back}	1 mm [14]
Impeller surface roughness	k_R	2 µm [14,28]
Diffuser width ratio	$\frac{b_2}{b_5}$	1

The design is chosen under the constraint of the required total pressure ratio, Π_{tt}, by maximising the isentropic efficiency. Further boundaries for the design process are chosen according to Aungier [29], Van den Braembussche [30], Casey and Robinson [31], Japikse und Baines [32], Lüdtke [33] and Whitfield and Baines [34].

The Euler Equation,

$$a_u = c_{u2}u_2 - c_{u1}u_1, \tag{6}$$

defines the work capacity of the impeller by using the circumferential component of the absolute velocities, c_{u1} and c_{u2}, and the circumferential velocities, u_1 and u_2, at the impeller inlet and outlet, respectively. The ratio of the total enthalpy difference, $\Delta h_{s.tt}$, achievable under isentropic change of state, and the actual circumferential work determined the isentropic total-to-total efficiency,

$$\eta_{s.tt} = \frac{\Delta h_{s.tt}}{a_u}, \tag{7}$$

of the compressor. For the diffuser, adiabatic conditions are assumed, and therefore $h_{2.t} = h_{5.t}$. To calculate the runner outlet, the slip factor,

$$\sigma = 1 - \frac{\Delta c_{u2}}{u_2}, \tag{8}$$

based on the empirical approach of Wiesner [35] is used. Due to the finite number of blades, the flow cannot follow the blade contour completely. The slip factor therefore takes into account the deviation between relative flow and metal angle at the outlet of the impeller.

The losses in the compressor impeller are considered in the design by means of common and known loss correlations, which are summarized in Table 5. However, losses at the inlet guide vanes are not considered. A geometry is calculated for the given design point. The off design behaviour for the geometry is determined by varying the operating conditions. The final result is the compressor map showing the total-to-total pressure ratio and isentropic total-to-total efficiency achievable at a given speed and mass flow. If the mass flow is reduced, the compressor soon reaches the surge limit. However, this is extremely difficult to determine. In this model, the mass flow at which the static-to-static pressure ratio becomes maximum was assumed to be the surge limit of the system. As the mass flow increases, the impeller inlet or outlet soon become choked. The flow velocity then reaches the value of the speed of sound of the refrigerant, and the mass flow cannot be increased any further.

Table 5. Loss correlations.

Name	Variable	Value
Incidence Loss	$\Delta h_{inc} = \frac{1}{2} w_1^2 \sin(\beta_{1.opt} - \beta_1)$	Galvas [36]
Skin Friction Loss	$\Delta h_{sf} = 4 C_f \frac{L_h}{d_H} \bar{w}_1{}^2$	Galvas [36]
Diffusion & Blade Loading Loss	$\Delta h_{bl} = 0.05 D_f^2 u_2^2$	Coppage & Dallenbach [37]
Clearance Loss	$\Delta h_{bl} = 0.6 \frac{\bar{\epsilon}}{b_2} \lvert c_{u2} \rvert \sqrt{\frac{4\pi}{b_2 Z} \frac{r_{1sh}^2 - r_{1h}^2}{(r_2 - r_{1sh})(1 + \frac{\rho_2}{\rho_1})} \lvert c_{u2} \rvert c_{m1}}$	Jansen [38]
Mixing Loss	$\Delta h_{mix} = \frac{1}{1 + \tan^2(\alpha_2)} \left(\frac{\epsilon_w}{1 - \epsilon_w} \right)^2 \frac{c_2^2}{2}$	Johnston & Dean [39]
Disk Friction Loss	$\Delta h_{df} = 0.25 \frac{\bar{\rho} u_2^3 r_2 K_f}{\dot{m}} \left(\frac{\epsilon_w}{1 - \epsilon_w} \right)^2 \frac{c_2^2}{2}$	Daily & Nece [40]
Recirculation Loss	$\Delta h_{rc} = 0.02 D_f^2 u_2^2 \sqrt{\tan(\alpha_2)}$	Coppage & Dallenbach [37]

2.4. Performance Map Fitting

In order to implement the detailed compressor model described in the previous section into the system simulation of the whole heat pump, a data-driven surrogate model of the compressor is obtained. The surrogate model is identified according to the ALVEN algorithm proposed by Sun and Braatz [41], although ultimately different feature selection methods were used. ALVEN builds an elastic-net linear regression model following non-linear feature transformation and generation and two-step feature selection. The raw data for each compressor are available as a sparse performance map for dimensionless mass flow ($\dot{m}_d$) and pressure ratio (Π_{tt}) variables with the efficiencies calculated for certain rotational frequencies. The variables are transformed non-linear, including 1st- and 2nd-order interaction terms, which are shown in Table 6.

Table 6. Nonlinear terms for the performance map fitting with $i = \dot{m}_d, \Pi_{tt}$.

1st-order terms					
x_i	$\sqrt{x_i}$,	$\log x_i$	$\frac{1}{x_i}$		
2nd-order terms					
x_i^2	$x_i^{3/2}$	$(\log x_i)^2$	$\frac{\log x_i}{x_i}$	$\frac{1}{x_i^2}$	$x_i^{-1/2}$

The resulting 21 features are then reduced by a variance threshold and scaled and centred by standard deviation and sample mean value. The second feature selection step is performed by recursive feature elimination using a support vector regression model. Finally, additional features are eliminated by the L1-Norm of the elastic-net model. Each step is implemented in a *scikit-learn* [42] pipeline using standard components, except for the non-linear transformation, which is a custom implementation. Before fitting, all data sets are shuffled and split in a 80/20 training and test set ratio. The splitting is performed using a stratified method in which the continuous target variable is divided into six bins.

The calculated compressor map is based on given constant inlet temperature and inlet pressures. If the actual inlet conditions regarding temperature or pressure differ from the design point, the same mass flow results in a different volume flow and different velocities. Subsequently, the compressor map is no longer replicating the actual performance of the compressor. Therefore, varying inlet conditions are compensated using reduced numbers and a corrected mass flow $\dot{m}_{corr}$. Equation (9) is used as an input to the compressor performance model to obtain actual efficiencies.

$$\dot{m}_{corr} = \dot{m} \frac{p_{DP.t1} \sqrt{T_{t1}}}{p_{t1} \sqrt{T_{DP.t1}}} \tag{9}$$

3. Results

3.1. Refrigerant Selection

The pressure ratio between the evaporator pressure and high pressure is an important limitation for the turbo compressor because, around $\Pi_{ttStage} = 2.5$, it becomes difficult to find a sufficient design. Figure 5 shows the COP depending on the pressure ratio per stage for the most promising refrigerants. In the simulation, a temperature spread of 15 °C is applied in the IHEX. The overall highest efficiency was achieved using Cyclopentane, but also with the highest pressure ratio of approximately 2.7 per stage. In the case of two compressors, this would lead to very high compressor speeds and unfavourable dimensions, such as small b_2, which lead to poorer compressor efficiencies. The solution to this problem would be the introduction of a 3rd stage, but this would have disadvantages of increasing costs of approximately 50%. The second best option would be Pentane (R601), with a COP of approximately 2.9, but again with a critical Π_{Stage}. Therefore, refrigerant blends are designed with the intention of improving the behaviour. As discussed in [16], the blends did not live up to the expectations. With Pentane being a more challenging option in many ways, it was decided to use R1233zd(E), with the 3rd highest COP and a favourable $\Pi_{ttStage}$ of approximately 2.3.

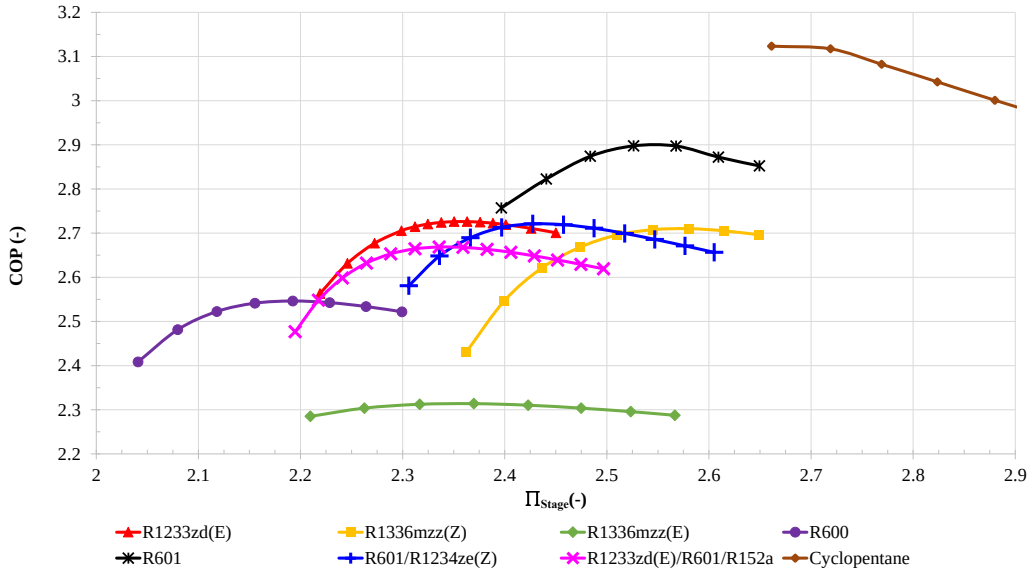

Figure 5. COP over pressure ratio per stage for different refrigerants.

3.2. Compressor Design

The resulting geometry and design variables of the preliminary compressor design for R1233zd(E) are shown in Table 7. There are two different designs depending on the use of inlet guide vanes with a fixed angle of $\alpha_1 = 30°$ or without guide vanes, assuming zero inlet swirl.

In the design point, compressor 1 reaches a total-to-total isentropic efficiency of 0.68 without guide vanes and approximately 0.79 with fixed inlet guide vanes. In the case of compressor 2, it is 0.61 and 0.74, respectively. This corresponds to an improvement of approximately 21% and 16% by means of using inlet guide vanes.

Figure 6 shows the preliminary design of the radial compressor for R1233zd(E). On the left-hand side, a meridian view of both compressor impellers is depicted. The right-hand side shows a 3D sketch of compressor 1. Therefore, the intersectional blade angles on the leading edge are approximated, exponentially increasing from hub to shroud.

Table 7. Data for the R1233zd(E) radial compressors.

Geometry	**Compressor 1**		**Compressor 2**	
α_1 (°)	0	30	0	30
Π_{tt}(-)	2.37	2.38	2.38	2.35
$\dot{m}$ ($\frac{kg}{s}$)	6.36	6.36	6.36	6.36
$\eta_{s.tt}$ (-)	0.684	0.785	0.614	0.74
P (kW)	192.3	167.3	208.1	167.2
p_{t1} (bar)	8.33	8.33	19.74	19.67
T_{t1} (K)	423.2	423.2	464	460
d_2 (m)	0.145	0.144	0.102	0.099
n ($\frac{rev}{min}$)	26,700	26,500	38,500	37,700
Z (-)	20	20	20	22
u_2 ($\frac{m}{s}$)	203	200	206	195
$\frac{r_{1sh}}{r_2}$(-)	0.5	0.5	0.5	0.5
$\frac{r_{1h}}{r_{1sh}}$(-)	0.5	0.5	0.5	0.5
$\frac{b_2}{r_2}$(-)	0.1	0.1	0.1	0.1
r_5 (m)	0.13	0.13	0.094	0.088
β_{2b} (°)	−40	−40	−35	−40
L_{ax} (m)	0.0497	0.0476	0.0386	0.0327

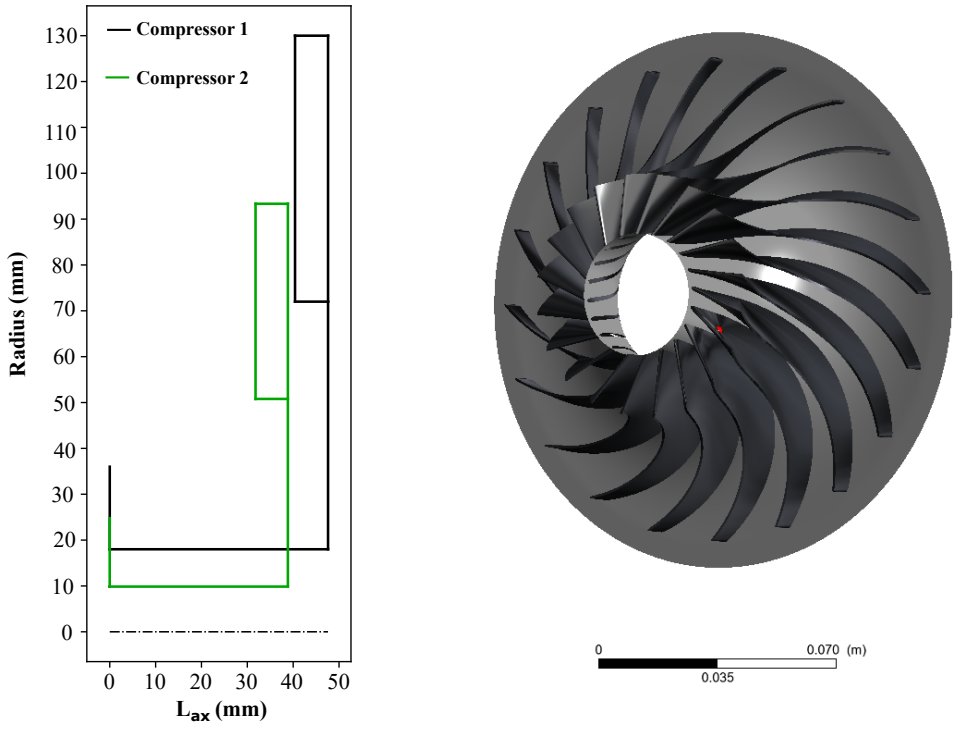

(a) (b)

Figure 6. Preliminary compressor design for R1233zd(E): (**a**) meridian view and (**b**) CAD sketch.

Figure 7 shows the compressor maps of the two compressors. Depending on mass flow and speed, the expected isentropic total-to-total efficiency can be determined. The black cross marks the location of the design point. For the compressors with additional guide vane rows at a fixed position, a clear extension of the operating range can be seen. If the compressors are encountering a positive inlet swirl, there is a reduction in the relative inlet velocity. Therefore, chocking occurs only at a higher mass flow rate. Smaller inlet velocities also reduce friction and viscous flow losses in the impeller and increase efficiency. However, a guide vane series is associated with additional costs and, in the case of adjustable guide vanes, with additional control engineering effort. It is therefore necessary to assess whether the installation of such an additional part would actually be beneficial.

It is also worth mentioning that for all compressors the highest efficiency is not achieved in the design point, which is marked by a black cross, but in part load. This highly depends on the loss correlations and can be changed or accurately adjusted. In our case, the 1D modelling of the vaneless diffuser leads to over prediction by not taking the actual length of the streamlines into account. To improve that behaviour, a 2D approach solving the radial and tangential momentum, mass continuity and energy balance for the diffuser has to be applied. In general, it is beneficial to select a design point not too close to the threshold of the operating limit as the heat pump shall be able to operate in off-design.

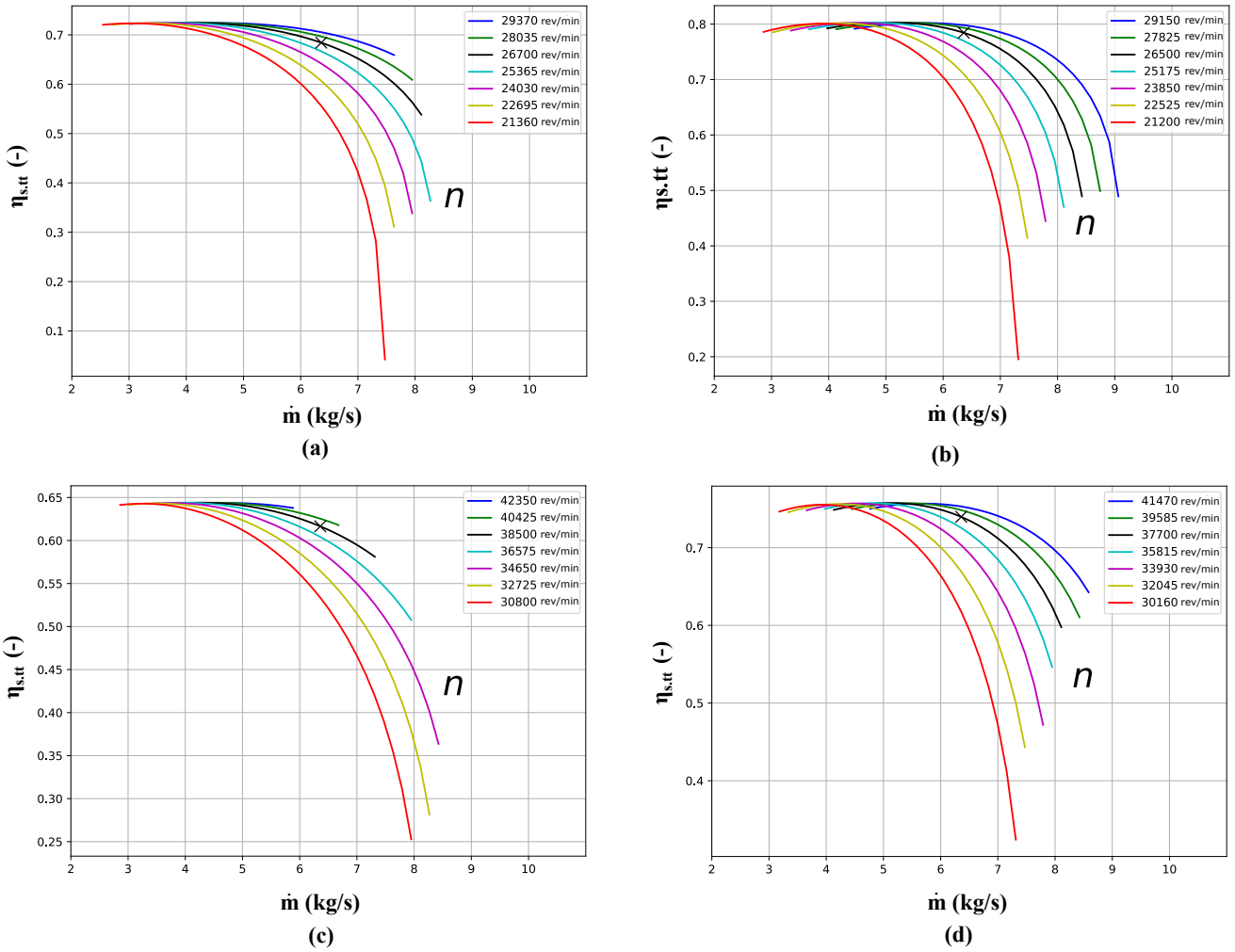

Figure 7. Isentropic total-to-total efficiency curves for compressor 1, (**a**) without guide vanes and (**b**) with guide vanes, and for compressor 2, (**c**) without guide vanes and (**d**) with guide vanes.

3.3. Performance Map Fitting

Table 8 shows the median absolute percentage error (MedAPE), the maximal absolute percentage error (MaxAPE) on the test set and the final number of model parameters obtained for the surrogate model of the performance map. Maximal model errors were generally observed at the lowest efficiencies.

The identified equations and parameters of the elastic-net model for each compressor are implemented into the Dymola/Modelica model. To ensure that further simulations are within the valid range of the surrogate model, the edge values of the performance map are detected and fitted with polynomial curves. Simulated values can then be checked to be

either above or below those edge curves accordingly. The identified model equations and parameters are presented in Equation (10) and Table 9

$$\eta = \sum a_i \frac{f_i - \mu_i}{\sigma_i} \tag{10}$$

Table 8. Results for data-driven performance map fitting.

Compressor	Datapoints	MedAPE, %	MaxAPE, %	Num. Params
Compressor 1	761	0.42	2.21	6
Compressor 2	669	0.39	7.67	7
Compressor 1 with guide vanes	750	0.48	5.62	8
Compressor 2 with guide vanes	675	0.33	2.84	8

Table 9. Identified parameters for performance map fitting.

	Compressor 1			Compressor 2			Compressor 1 α_1			Compressor 2 α_1		
f_i	a	μ	σ	a	μ	σ	a	μ	σ	a	μ	σ
1	0.658	0	0	0.591	0	0	0.74	0	0	0.706	0	0
$\Pi_{tt}\dot{m}$	0.072	12.0	3.60	0.053	11.5	2.88	0.095	12.4	3.57	0.098	12.5	3.54
$\log(\Pi_{tt})$	−0.163	0.756	0.244	−0.121	0.717	0.226	−0.219	0.736	0.237	−0.198	0.735	0.227
$\log(\dot{m})$	0	0	0	0	0	0	0.015	1.74	0.255	0.008	1.75	0.225
Π^2	0.014	5.08	2.43	0.012	4.65	2.15	0.022	4.86	2.30	0.018	4.81	2.19
$\dot{m}^2$	−0.100	33.3	15.9	−0.086	33.4	15.7	−0.133	36.7	17.0	−0.114	36.7	15.1
$(\log(\Pi_{tt}))^2$	0	0	0	−0.010	0.565	0.332	−0.002	0.598	0.351	−0.004	0.592	0.336
$\frac{1}{\Pi_{tt}^2}$	−0.150	0.250	0.131	−0.109	0.263	0.120	−0.179	0.257	0.128	−0.153	0.254	0.120

3.4. Heat Pump Design

The interaction of the designed compressors with the other components of the heat pump is investigated using the described heat pump simulation model. The operating parameters of the design point are summarized in Table 1. In the simulations, pressurized water cycles at the source and the sink are assumed. However, another sensible heat-transfer medium at the sink, such as thermal oil or direct heating of air, would also be possible. As can be seen in the log(p)-h-diagram for the design point, depicted in Figure 8, the heat pump operates transcritically with a temperature glide at the gas cooler. As a result, the high-pressure level does not depend on the two-phase equilibrium but can be varied within a reasonable range. The chosen high-pressure level impacts the COP of the heat pump, and the optimum high-pressure level to achieve the maximum possible COP differs for varying operating conditions. However, the size of the internal HEX has an even bigger impact. The more heat transferred in the internal HEX, the higher the COP. To keep all simulations comparable to each other, the minimum temperature difference between the cold and the hot side is set constant to 15 °C.

Besides the resulting COP for different high-pressure levels, the off-design behaviour is of special interest. The part-load and over-load factor is defined using the thermal capacity at the sink. The investigated range of 50 to 130% capacity corresponds to a thermal power of 0.5 MW up to 1.3 MW, whereby the sink outlet temperature is always kept constant at 200 °C. Depending on the consumer and the implementation of the water cycle at the sink, reducing or increasing the thermal power can result in the two following scenarios:

- Scenario 1 with constant return flow temperature: In Scenario 1, the return flow temperature, $T_{sink,in}$, is held constant and the water mass flow at the sink, $\dot{m}_{water,sink}$, is adjusted, so that the targeted part-load or over-load factor is achieved. This means that 50% capacity corresponds to half of the water mass flow.
- Scenario 2 with constant water mass flow: In Scenario 2, the water mass flow at the sink, $\dot{m}_{water,sink}$, is set to be constant. This results in an increasing return flow

temperature, $T_{sink,in}$, at decreasing thermal power. This means that 50% capacity corresponds to a return flow temperature of 180 °C.

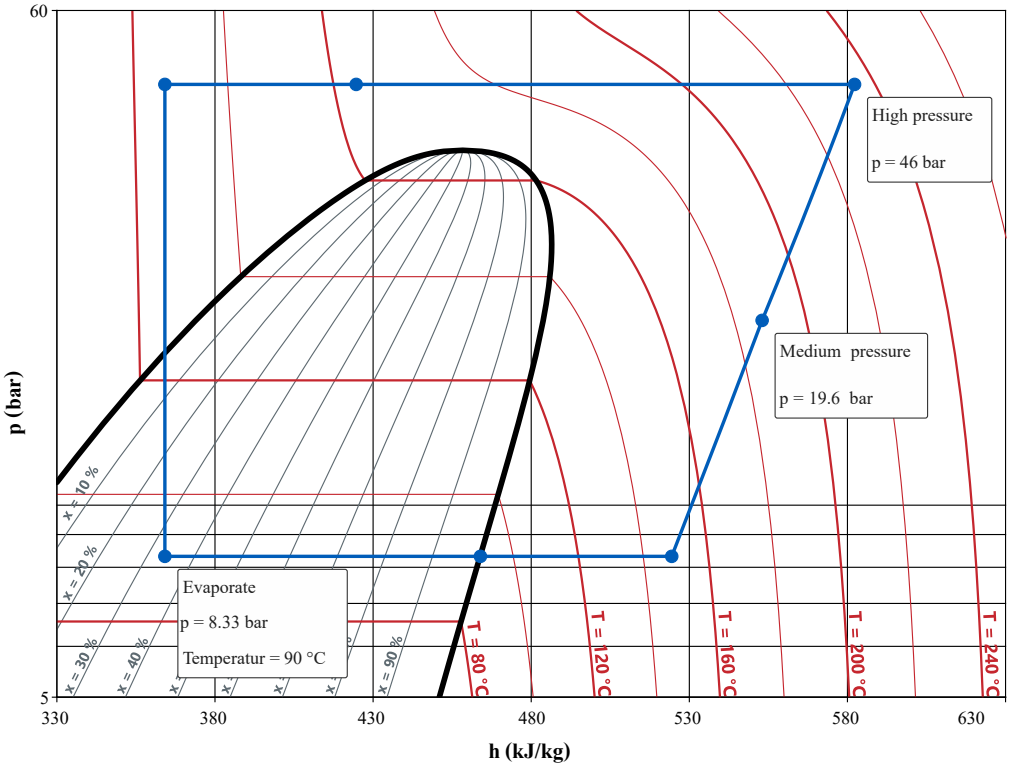

Figure 8. Log(p)/h diagram of the reference cycle.

The resulting COP for these two scenarios using compressors with and without inlet guide vanes is depicted in Figure 9a–d. The grey areas in the gird represent operation conditions outside of the operation area of at least one compressor, left of the surge line or right of the choke line. For all scenarios, the heat pump using the compressors with inlet guide vanes performs better due to the better compressor efficiency. Furthermore, the operating area using the compressor with inlet guide vanes is larger. While in Scenario 2 the COP is significantly decreasing in part-load, for Scenario 1 it is slightly improved. Finally, the behaviour of the heat pump in the case of a decreased source temperature, $T_{source,in}$, using Scenario 1 is also investigated. As decreasing the source temperature results in a lower compressor inlet pressure, a higher pressure ratio is needed to reach the same pressure level at the compressor outlet. The results for a source temperature of 85 °C, leading to an evaporation temperature of 80 °C, are depicted in Figure 9e using the compressors without inlet guide vanes and Figure 9f using the compressors with inlet guide vanes. As a result of the increased temperature lift, the COP is decreased. Additionally, the increased pressure ratio limits the valid operation are, and over-load operation is no longer possible.

Using the compressor maps, the required rotational speed for different operating points can be determined. In Figure 10, the selected operating points of the discussed scenarios are marked in the compressor maps of the four compressors. Inlet conditions varying from the design conditions are thereby considered as described in Section 2.4. The design point is marked with a red circle and the selected operating points with numbered crosses, which are explained in Table 10. It can be seen that the part-load is limited by the surge line of the second compressor and the over-load is limited by the maximum rotational speed of the first compressor using compressors with inlet guide vanes and the choke line of the second compressor for those without inlet guide vanes.

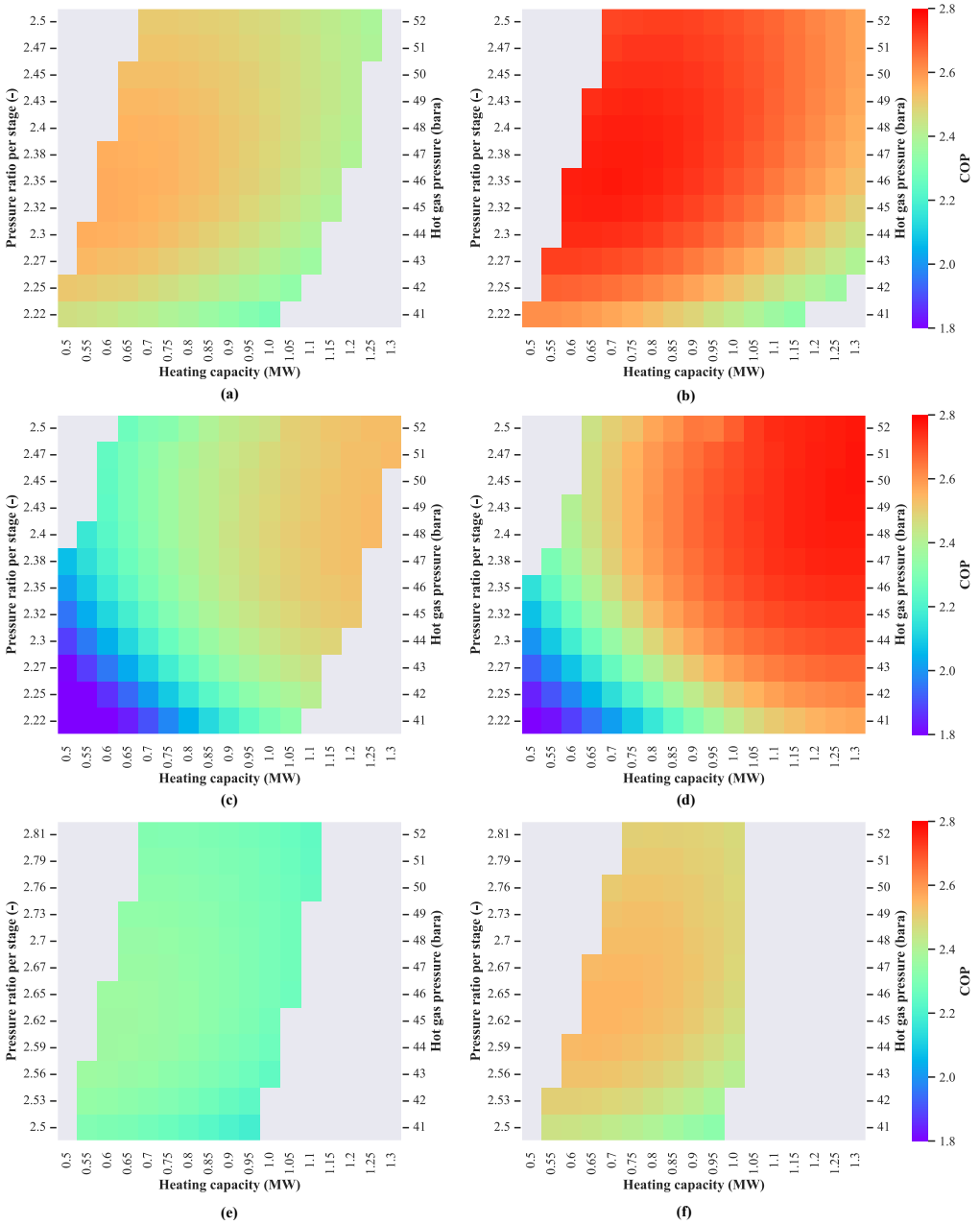

Figure 9. COP depending on part-load factor and high-pressure level for Scenario 1 (**a**,**b**), Scenario 2 (**c**,**d**), decreased source temperature (**e**,**f**) and compressors without inlet guide vanes (left column) and with inlet guide vanes (right column).

Table 10. Selected operating points.

	Description
x_1	minimum part load with Scenario 1
x_2	maximum over load with Scenario 1
x_3	minimum part load with Scenario 2
x_4	maximum over load with Scenario 2
x_5	maximum over load with decreased source temperature
x_6	minimum part load with decreased source temperature

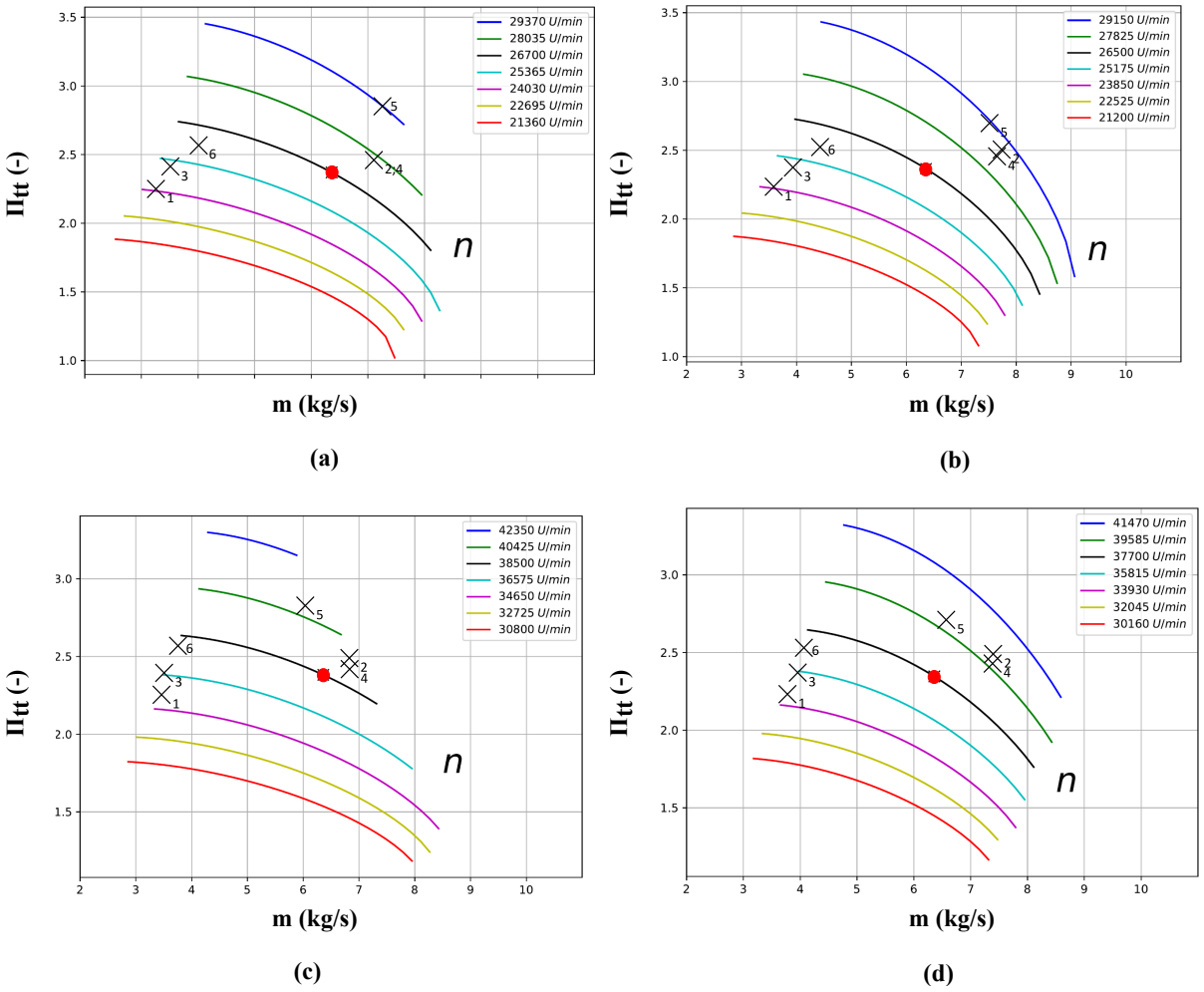

Figure 10. Compressor maps for compressor 1 (**a**) without guide vanes and (**b**) with guide vanes and compressor 2 (**c**) without guide vanes and (**d**) with guide vanes.

4. Use Case Study

As a use case for the heat pump, a deep fryer is presented in Figure 11. Potatoes are chopped, and the chips are than fried by oil. Thereby, the potato chips evaporate water and absorb oil. As a consequence, new oil has to be pumped into the system in order to keep the fluid level constant. This additional oil stream is mixed with the return oil, which is cooled down to 170 °C during the process. The resulting oil stream has to be heated up to 200 °C for frying the potato chips.

The process is analysed by means of a pinch analysis, which is one of the most common process integration techniques [43]. This is a structured and continuous processes applicable approach that can be used to screen the potentials for different heating technologies, such as, for example, the heat pump would be. Wu et al. [44] showed the applicability for a similar case of a potato fryer but with the goal to estimate the energy efficiency of the system. Figure 11b shows the resulting composite curves for the use case. The available hot stream is the water, which evaporates during the frying process. The cold stream requires a total amount of heat of approximately 1 MW_{th}, with a very small amount of recoverable heat at approximately 15 kW_{th} by means of direct heat recovery.

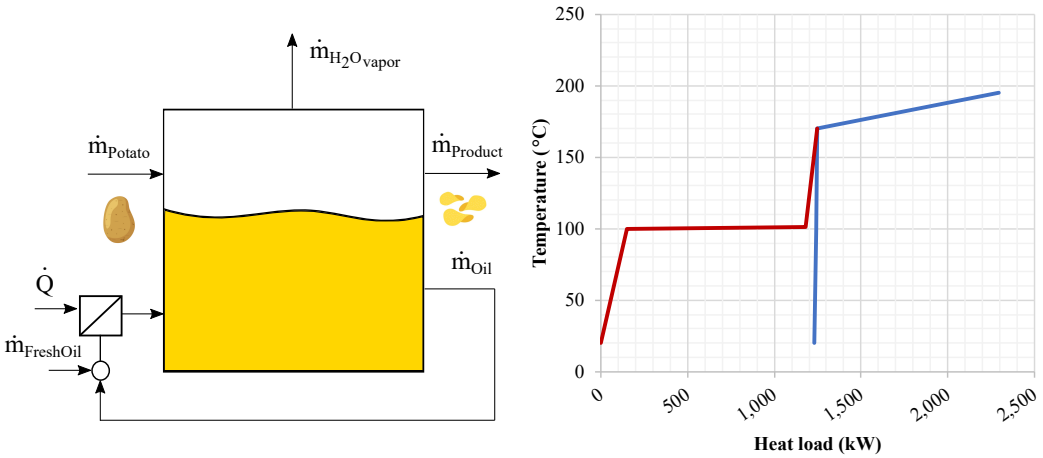

Figure 11. (**a**) Schematic drawing of the deep fryer and (**b**) composite curve.

The resulting grand composite curve is shown in Figure 12a. The remaining heat after direct heat recovery is covered by the designed high-temperature heat pump. The blue and red vertical lines in the diagram mark the temperatures and heat loads of the evaporator as well as the condenser. On the right-hand side (Figure 12b), a schematic drawing of the heat pump including heat load is shown. Moreover, the assumed costs for the main parts of the heat pump are displayed. The most difficult part is estimating the compressor costs. As this part had never been built before, an estimation based on various assessments published in the literature [33,45,46] and own experience was carries out. The displayed costs in Figure 12 include costs for a mechanical gearbox and an electrical drive system as well as a frequency converter. The option for a direct electrical drive via an axial-flux motor would probably be the best solution, but as such machines are still tailor-made solutions and subject to research and development they are not chosen for this cost analysis.

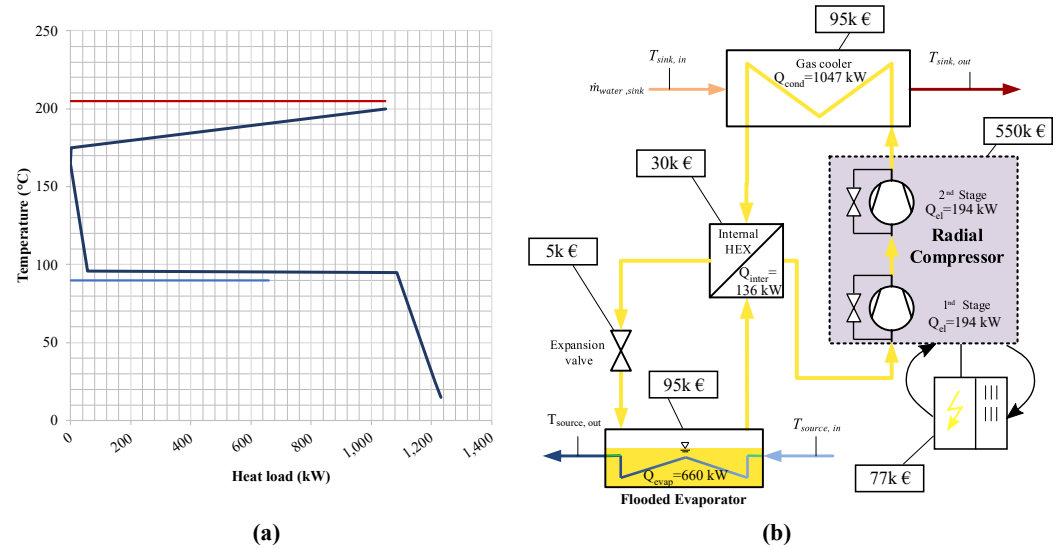

Figure 12. (**a**) Grand composite curve and (**b**) schematic drawing of the heat pump, including cost estimations for main components.

Overall, a value of EUR 970/kW$_{th}$ was assumed for the capital expenses (CAPEX) of the heat pump. The operation and maintenance expenses (OPEX) are assumed to be around 5.5% of the CAPEX [7]; CO_2 pricing is taken into account with a value of EUR 100/ton$_{CO_2eq}$ according to [47].

In Figure 13, the payback time of the heat pump with reasonable electricity-to-gas-price ratios (EGPR) is depicted. It can be seen that with a low EGPR, which is common in Scandinavia or even somewhat higher, as is the case in Central Europe, the heat pump CAPEX would lead to attractive payback periods of approximately 2–10 years. However, uncertainties in both directions, such as the actual integration costs as well as opportunities for funding, have to be taken into account for a more detailed analysis.

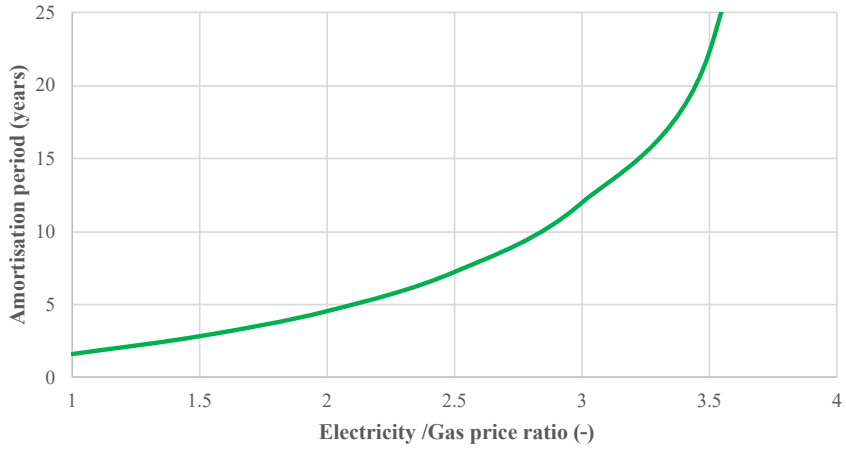

Figure 13. Payback time for different electricity-to-gas-price ratios.

5. Conclusions and Outlook

This paper presents a design approach for an industrial heat pump of approximately 1 MW, supplying sink temperatures of 200 °C. It is also worth noting that the goal was not to produce process steam but to heat air for drying or to heat up oil or pressurized water. A simple thermodynamic cycle model of the heat pump is used to optimize the COP for different refrigerants. The most promising solution is than passed to a mean-line compressor model, which suggests a preliminary design for both compressor stages. Afterwards, a prediction of the off-design behaviour is performed by loss correlations. To include the compressor map in the heat pump model, a data-driven surrogate model is obtained. This approach enables detailed heat pump simulations on a system level. It is intended to facilitate heat pump development for higher source temperatures using oil-free radial compressors. The best performing refrigerant, Cyclopentane, is not used as the pressure ratio is too high for a two-stage compressor design. Therefore, Pentane and the HFO R1233zd(E) are the most promising candidates. R1233zd(E) is than chosen based on the more sufficient pressure ratio and lower security class. For the design point, a total-to-total isentropic efficiency of approximately 0.79 and 0.74 for the second stage was reached. Both these values correspond to the use of inlet guide vane, which improves the efficiency by 21% in the first stage and 16% in the second stage. The surrogate model, which is used to transform the preliminary compressor design to the heat pump simulation environment, achieved an average error of beneath 0.5%, with a maximum value of 7.67% deviation.

In the heat pump simulations, a maximum COP of 2.8 is achieved using both compressors with fixed guide vanes at 30 °C. The use case of a deep fryer showed the feasibility concept, even taking into account economic aspects. With estimated CAPEX of approximately EUR 970/kW_{th}, attractive payback periods of approximately 2–10 years were reached considering electricity to gas price ratios from 1 to approximately 3.

The overall goal is to build up the investigated heat pump cycle and test it under laboratory conditions to prove the promising results of this study. However, there are several simplifications made in the design and analysis, which require further work on the heat pump cycle and the compressor design.

- The chosen 1D single-zone mean-line approach only provides a preliminary compressor design. In order to produce both compressor stages, a more detailed design of all compressor parts, including such things as spiral casing and guide vanes, would be necessary.
- The 1D diffuser model is fast but leads to over-prediction of the efficiencies at part-load. Therefore, a 2D model would be more sufficient.
- The simulated heat pump cycle is lacking a refrigerant-regulating component, such as a refrigerant accumulator, which will be necessary for the circuit design to react to varying evaporation or high-pressures. This problem could be faced by an expansion in two stages and by adding a flash tank in between or a flooded evaporator.
- In this study, only steady state operation is investigated. For full realisation, a control strategy and a start-up strategy should be developed.

Moreover, for a new development, a manufacturer could also focus on Pentane as a refrigerant because at this time synthetic refrigerants are discussed quite critically and the development will take some time.

Author Contributions: Conceptualization, J.U., V.S. and R.W.; methodology, C.K., R.J., V.S., R.W. and J.U.; software, C.K. and R.J.; formal analysis, J.U.; investigation, C.K., J.R., R.J., J.U. and V.S.; resources, R.W. and J.U.; data curation, J.U.; writing—original draft preparation, J.U., R.J. and V.S.; writing—review and editing, J.U., V.S. and R.W.; visualization, J.U. and C.K.; supervision, R.W.; project administration, J.U.; funding acquisition, J.U. and R.W. All authors have read and agreed to the published version of the manuscript.

Funding: The authors acknowledge TU Wien Bibliothek for financial support through its Open Access Funding Programme. This work was conducted within the project "NERO" (FFG project number: 888453). This project is funded by the Climate and Energy Fund and is carried out within the framework of the Energy Research Program 2020 of the Austrian national Research Funding Agency (FFG).

Conflicts of Interest: The authors declare no conflict of interest.

Abbreviations

Acronyms

CAPEX	Capital expenses
COP	Coefficient of performance
HEX	Heat exchanger
OPEX	Operation and maintenance expenses

Parameters

α	Guide vane angle (°)
β	Blade angle (°)
Δ h	Enthalpy Deviation ($\frac{kJ}{kg}$)
ϵ	Gap distance (m)
η	Efficiency (-)
Π	Pressure ratio (-)
σ	Slip factor (-)
ω	Angular velocity (s^{-1})
d	Diameter or Wide (m)
h	Enthalpy ($\frac{kJ}{kg}$)
L	Length (m)
$\dot{m}$	Mass flow ($\frac{kg}{s}$)
n	Rotational speed (rpm)
P	Power (kW))
r	Radius (m)
T	Temperature (K)
x	Parameter
Z	Number of blades (-)

Subscripts	
1	Impeller inlet
2	Impeller outlet
5	Diffuser outlet
ax	Axial
b	Blade
bl	Blade loading
back	Backstep
Corr	Correction
DP	Design Point
df	Disk friction
evap	Evaporation
h	Hub
i	Counting Indices
in	Incoming
inc	Incidence
mix	Mixing
out	Outgoing
t	Total
R	Surface Roughness
rc	Recirculation losses
rms	Root mean square
s	Isenctropic
sf	Skin friction
sh	Shroud
therm	Thermal
u	Circumferential
hp HP	Heat pump

References

1. European Commision. 2030 Climate & Energy Framework. 2021. Available online: https://ec.europa.eu/clima/policies/strategies/2030_en (accessed on 10 April 2023).
2. IEA—International Energy Agency. World Energy Outlook 2021. 2021. Available online: https://www.iea.org/reports/world-energy-outlook-2021 (accessed on 10 April 2023).
3. Papapetrou, M.; Kosmadakis, G.; Cipollina, A.; La Commare, U.; Micale, G. Industrial waste heat: Estimation of the technically available resource in the EU per industrial sector, temperature level and country. *Appl. Therm. Eng.* **2018**, *138*, 207–216. [CrossRef]
4. Lecompte, S.; Huisseune, H.; Van Den Broek, M.; Vanslambrouck, B.; De Paepe, M. Review of organic Rankine cycle (ORC) architectures for waste heat recovery. *Renew. Sustain. Energy Rev.* **2015**, *47*, 448–461. [CrossRef]
5. Kosmadakis, G.; Arpagaus, C.; Neofytou, P.; Bertsch, S. Techno-economic analysis of high-temperature heat pumps with low-global warming potential refrigerants for upgrading waste heat up to 150 °C. *Energy Convers. Manag.* **2020**, *226*, 113488. [CrossRef]
6. Kosmadakis, G. Estimating the potential of industrial (high-temperature) heat pumps for exploiting waste heat in EU industries. *Appl. Therm. Eng.* **2019**, *156*, 287–298. [CrossRef]
7. Arpagaus, C. *Hochtemperatur-Wärmepumpen–Marktübersicht*; Stand der Technik, Anwenderpotenziale; VDE-Verlag GmbH, Berlin–Offenbach: Offenbach am Main, Germany, 2019.
8. Wilk, V.; Lauermann, M.; Helminger, F. Decarbonization of industrial processes with heat pumps. In Proceedings of the 25th IIR International Congress of Refrigeration, Montreal, QC, Canada, 24–30 August 2019.
9. Helminger, F.; Hartl, M.; Fleckl, T.; Kontomaris, K.; Pfaffl, J. Hochtemperatur Wärmepumpen Messergebnisse einer Laboranlage mit HFO-1336MZZ-Z bis 160° C Kondensationstemperatur. In Proceedings of the 14th Symposium Energieinnovation, Graz, Austria, 10–12 February 2016; Volume 10, p. 12.
10. Wang, K.; Cao, F.; Wang, S.; Xing, Z. Investigation of the performance of a high-temperature heat pump using parallel cycles with serial heating on the water side. *Int. J. Refrig.* **2010**, *33*, 1142–1151. [CrossRef]
11. Shen, Q.; Zhou, Z.; Li, S.; Liao, X.; Wang, T.; He, X.; Zhang, J. Design and analysis of the high-speed permanent magnet motors: A review on the state of the art. *Machines* **2022**, *10*, 549. [CrossRef]
12. Schiffmann, J.; Favrat, D. Design, experimental investigation and multi-objective optimization of a small-scale radial compressor for heat pump applications. *Energy* **2010**, *35*, 436–450. [CrossRef]
13. Hanslik, F.; Suess, J. Water as a Refrigerant in Centrifugal Compressor Cooling Systems for Industrial Applications. In *Advanced Cooling Technologies and Applications*; IntechOpen: London, UK, 2018.

14. Meroni, A.; Zühlsdorf, B.; Elmegaard, B.; Haglind, F. Design of centrifugal compressors for heat pump systems. *Appl. Energy* **2018**, *232*, 139–156. [CrossRef]
15. Harley, P.; Spence, S.; Filsinger, D.; Dietrich, M.; Early, J. An evaluation of 1D design methods for the off-design performance prediction of automotive turbocharger compressors. In Proceedings of the Turbo Expo: Power for Land, Sea, and Air, Copenhagen, Denmark, 11–15 June 2012; Volume 44748, pp. 915–925. [CrossRef]
16. Sulzgruber, V.; Riedl, J.; Unterluggauer, J. Concept study for industrial heat pumps up to 250° C heat sink temperature using radial turbo compressors. In Proceedings of the 13th Internationale Energiewirtschaftstagung an der TU Wien, Vienna, Austria, 15–17 February 2023.
17. Lemmon, E.W.; Bell, I.H.; Huber, M.L.; McLinden, M.O. NIST Standard Reference Database 23: Reference Fluid Thermodynamic and Transport Properties-REFPROP, Version 10.0, National Institute of Standards and Technology. 2018. Available online: https://www.nist.gov/srd/refprop (accessed on 14 April 2023). [CrossRef]
18. Helminger, F.; Unterluggauer, J.; Riedl, J. Hochtemperaturwärmepumpen bis zu 250 °C. Eine Konzeptstudie und EU-Forschungsvorhaben. In Proceedings of the DKV-Tagung Dresden, Dresden, Germany, 17–19 November 2021.
19. Fernández-Moreno, A.; Mota-Babiloni, A.; Giménez-Prades, P.; Navarro-Esbrí, J. Optimal refrigerant mixture in single-stage high-temperature heat pumps based on a multiparameter evaluation. *Sustain. Energy Technol. Assess.* **2022**, *52*, 101989. [CrossRef]
20. Bell, I.H.; Wronski, J.; Quoilin, S.; Lemort, V. Pure and pseudo-pure fluid thermophysical property evaluation and the open-source thermophysical property library CoolProp. *Ind. Eng. Chem. Res.* **2014**, *53*, 2498–2508. [CrossRef]
21. Lemmon, E.W.; Huber, M.L.; McLinden, M.O. *NIST Reference Fluid Thermodynamic and Transport Properties–REFPROP*, 7th ed.; NIST Standard Reference Database 23; National Institute of Standards and Technology: Gaithersburg, MD, USA, 2002.
22. Japikse, D. *Centrifugal Compressor Design and Performance*; Concepts ETI, Inc.: Wilder, VT, USA, 1996.
23. Cordier, O. Ähnlichkeitsbedingungen für Strömungsmaschinen. *BWK Bd* **1953**, *6*, 337–340.
24. Willinger, R. *Das CORDIER-Diagramm für Strömungsarbeitsmaschinen-Eine theoretische Begründung mittels Stufenkennlinien*; Bericht Nr.:2112; VDI Verlag GmbH: Düsseldorf, Germany, 2010.
25. Pfleiderer, C. *Strömungsmaschinen*; Springer: Berlin/Heidelberg, Germany, 2013.
26. Xu, C.; Amano, R.S. Empirical design considerations for industrial centrifugal compressors. *Int. J. Rotating Mach.* **2012**, *2012*, 184061. [CrossRef]
27. Traupel, W. *Thermische Turbomaschinen: Band 1: Thermodynamisch-strömungstechnische Berechnung*; Springer: Berlin/Heidelberg, Germany, 2019.
28. Chinnaswamy, S. The Impact of Surface Roughness on Transonic Compressor Performance. Master's Thesis, Department of Applied Mechanics, Chalmers University of Technology, Göteborg, Sweden, 2015; pp. 1652–8557.
29. Aungier, R.H. *Centrifugal Compressors: A Strategy for Aerodynamic Design and Analysis*; ASME Press: New York, NY, USA, 2000. [CrossRef]
30. Van den Braembussche, R. *Design and Analysis of Centrifugal Compressors*; John Wiley & Sons: Hoboken, NJ, USA, 2019.
31. Casey, M.; Robinson, C. *Radial Flow Turbocompressors*; Cambridge University Press: Cambridge, UK, 2021. [CrossRef]
32. Japikse, D.; Baines, N.C. *Turbomachinery Diffuser Design Technology*; Concepts Eti: White River Junction, VT, USA, 1998.
33. Luyben, W.L. Capital cost of compressors for conceptual design. *Chem. Eng. Process.-Process Intensif.* **2018**, *126*, 206–209. [CrossRef]
34. Whitfield, A.; Baines, N.C. Design of Radial Turbomachines. 1990. Available online: https://www.osti.gov/biblio/6550042 (accessed on 11 November 2022).
35. Wiesner, F. A review of slip factors for centrifugal impellers. *J. Eng. Power* **1967**, *89*, 558–566. [CrossRef]
36. Galvas, M.R. *Fortran Program for Predicting Off-Design Performance of Centrifugal Compressors*; Technical report NASA-TN-D-7487; NASA Lewis Research Center: Cleveland, OH, USA, 1973.
37. Coppage, J.; Dallenbach, F. *Study of Supersonic Radial Compressors for Refrigeration and Pressurization Systems*; Technical report; Garrett Corp Los Angeles Ca AiResearch MFG DIV: Los Angeles, CA, USA, 1956.
38. Jansen, W.; Moffatt, W.C. The Off-Design Analysis of Axial-Flow Compressors. *J. Eng. Power* **1967**, *89*, 453–462. [CrossRef]
39. Johnston, J.; Dean, R., Jr. Losses in vaneless diffusers of centrifugal compressors and pumps: Analysis, experiment, and design. *J. Eng. Power* **1966**, *88*, 49–60. [CrossRef]
40. Daily, J.W.; Nece, R.E. Chamber dimension effects on induced flow and frictional resistance of enclosed rotating disks. *J. Basic Eng. Mar.* **1960**, *82*, 217–230. [CrossRef]
41. Sun, W.; Braatz, R.D. ALVEN: Algebraic learning via elastic net for static and dynamic nonlinear model identification. *Comput. Chem. Eng.* **2020**, *143*, 107103. [CrossRef]
42. Pedregosa, F.; Varoquaux, G.; Gramfort, A.; Michel, V.; Thirion, B.; Grisel, O.; Blondel, M.; Prettenhofer, P.; Weiss, R.; Dubourg, V.; et al. Scikit-learn: Machine learning in Python. *J. Mach. Learn. Res.* **2011**, *12*, 2825–2830. [CrossRef]
43. Smith, R. State of the art in process integration. *Appl. Therm. Eng.* **2000**, *20*, 1337–1345. [CrossRef]
44. Wu, H.; Jouhara, H.; Tassou, S.; Karayiannis, T. Modelling of energy flows in potato crisp frying processes. *Appl. Energy* **2012**, *89*, 81–88. [CrossRef]
45. Turton, R.; Bailie, R.C.; Whiting, W.B.; Shaeiwitz, J.A. *Analysis, Synthesis and Design of Chemical Processes*; Pearson Education: London, UK, 2008.

46. Shamoushaki, M.; Niknam, P.H.; Talluri, L.; Manfrida, G.; Fiaschi, D. Development of cost correlations for the economic assessment of power plant equipment. *Energies* **2021**, *14*, 2665. [CrossRef]
47. Trading Economics. EU Carbon Permits. Available online: https://tradingeconomics.com/commodity/carbon (accessed on 12 February 2023).